Systematic Mapping of Icosahedral Short-Range Order in a Melt-Spun $Zr_{36}Cu_{64}$ Metallic Glass

A. C. Y. Liu,[1,2,*] M. J. Neish,[1,3] G. Stokol,[1] G. A. Buckley,[1] L. A. Smillie,[1] M. D. de Jonge,[4] R. T. Ott,[5] M. J. Kramer,[5,6] and L. Bourgeois[2,7]

[1]*School of Physics, Monash University, Clayton, Victoria 3800, Australia*
[2]*Monash Centre for Electron Microscopy, Monash University, Clayton, Victoria 3800, Australia*
[3]*School of Physics, University of Melbourne, Parkville, Victoria 3010, Australia*
[4]*Australian Synchrotron, Clayton, Victoria 3168, Australia*
[5]*Division of Materials Sciences and Engineering, Ames Laboratory, Ames, Iowa 50011, USA*
[6]*Department of Materials Science and Engineering, Iowa State University, Ames, Iowa 50011, USA*
[7]*Department of Materials Engineering, Monash University, Clayton, Victoria 3800, Australia*

(Received 20 August 2012; revised manuscript received 24 March 2013; published 17 May 2013)

By analyzing the angular correlations in scanning electron nanodiffraction patterns from a melt-spun $Zr_{36}Cu_{64}$ glass, the dominant local order was identified as icosahedral clusters. Mapping the extent of this icosahedral short-range order demonstrates that the medium-range order in this material is consistent with a face-sharing or interpenetrating configuration. These conclusions support results from atomistic modeling and a structural basis for the glass formability of this system.

DOI: 10.1103/PhysRevLett.110.205505 PACS numbers: 61.43.Fs, 61.05.jm, 64.70.pe, 81.05.Kf

Despite the lack of long-range order in metallic glasses (MGs), it is thought that significant localized atomic ordering exists. At the length scale of nearest-neighbor arrangements, the short-range atomic order (SRO) is dictated by efficient atomic packing in clusters or polyhedra [1]. The packing of these quasiequivalent clusters then gives rise to a distinct medium-range atomic order (MRO). Zr_xCu_{100-x} MGs have good glass-forming abilities over a wide range of compositions [2]. Modeling studies of this system using molecular dynamics (MD) [3,4] and reverse Monte Carlo (RMC) calculations [5] have identified the dominant SRO as Cu-centered icosahedral clusters using Voronoi analysis [3,5] and a cluster template method [4]. The incidence of icosahedra increases with increasing Cu content [3,5]. The short-range stability of icosahedral clusters in the liquid [6] contributes greatly to the slowing structural dynamics at the glass transition [3]. Icosahedral clusters in the models demonstrate a strong spatial correlation compared to other polyhedra, suggesting a string-like icosahedral MRO [5]. The percolation of this icosahedral network drives the system into dynamic arrest at the glass transition [7] and determines the glass's mechanical strength and brittleness [8]. In this Letter, we develop a quantitative nanodiffraction technique that provides strong verification of the SRO-MRO predicted by modeling and experimental support for frustrated packing of SRO clusters.

Conventional diffraction experiments measure volume-averaged two-body atomic correlations. In amorphous and glassy materials, the two-body correlations cannot distinguish between competing structural models and thus, do not permit deep insight into the influence of structure on properties [9]. Fluctuation electron microscopy (FEM) is a low spatial-resolution diffraction-based technique that is sensitive to higher-order atomic correlations and has been applied to characterizing the type and degree of order in many disordered materials [9]. Recently, FEM measurements have been used to refine atomic models using RMC calculations [9,10]. However, challenges in scaling experiment to simulation [9], limitations on model size [10], and insensitivity to differently quenched structures [11] suggest that complementary approaches be pursued. Using a subnanometer, coherent, and converged electron probe in a scanning transmission electron microscope, diffraction information can be obtained from volumes with a lateral length scale comparable to the SRO in MGs [12], potentially offering more direct measures of order. In the present study, we measure and map the magnitude of angular correlations in an array of scanning electron nanodiffraction (SEND[13,14]) patterns obtained from a $Zr_{36}Cu_{64}$ glass. We develop a statistical analysis and identify the predominant SRO in these materials as icosahedral clusters. Using further statistical measures, we infer that the MRO in this material consists of face-sharing or interpenetrating icosahedra in keeping with efficient space filling.

An as-spun melt-spun $Zr_{36}Cu_{64}$ glass was jet-polished until perforation (Struers TenuPol 5, 33.3%:66.7% nitric acid:methanol, $-40\,^{\circ}C$, 12 V, 100 mA), and then, briefly ion milled at low ion energies and temperature to remove the surface oxide (Gatan Precision Ion Polishing System, 5 min, 1 keV, $-100\,^{\circ}C$, 2° incident angle). The specimen was kept under vacuum and examined within 48 h of preparation to limit oxide formation. This preparation regimen did not result in any devitrification (see the Supplemental Material [15]). An FEI Titan^3 80-300 FEGTEM (300 keV) with C_s aberration correction of the imaging and probe-forming lenses was used to obtain SEND patterns of the

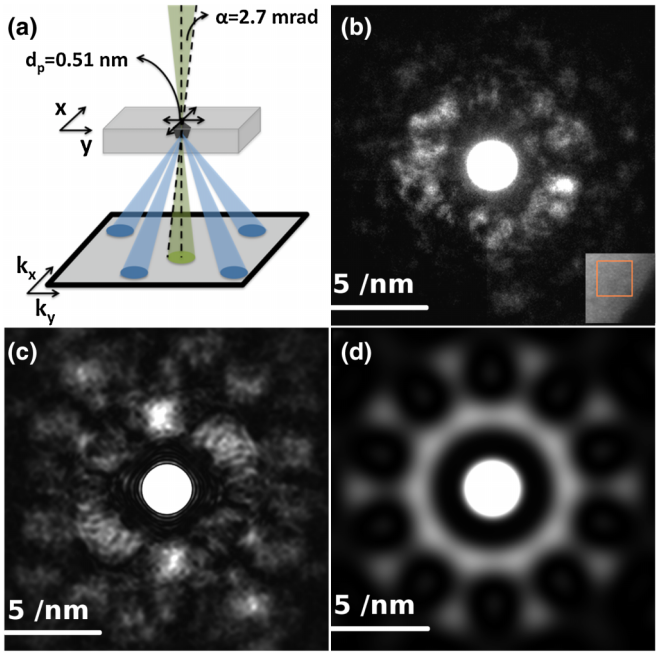

FIG. 1 (color online). (a) Schematic of SEND experiment. (b) Experimental SEND pattern and inset: HAADF image with boxed region (3 nm × 3 nm) where experimental SEND patterns were acquired. Simulated SEND patterns from (c) the model glass and (d) an icosahedral cluster aligned along the fivefold symmetry axis.

glass [Fig. 1(a): aperture semiangle $\alpha = 2.7$ mrad, spherical aberration $C_s = 0$ mm, defocus $\Delta f = 0$ nm, probe FWHM $d_p = 0.51$ nm]. These parameters were selected as an optimized compromise to bring the real space resolution (probe size) down to the size of SRO clusters (~0.6 nm) while still obtaining well-separated diffracted intensities. A high-angle annular dark-field (HAADF) reference image was used to select regions for investigation [inset Fig. 1(b)]. Arrays of 30 × 30 SEND patterns were collected from three 3.0 nm × 3.0 nm areas using a 1.5 s exposure time and a Gatan UltraScan CCD camera (2048 × 2048 binned to 512 × 512). Estimated thickness profiles were obtained using electron energy loss spectroscopy and the log-ratio technique [16] (see the Supplemental Material [15]). The thickness of the regions from which SEND patterns were obtained was ~5–10 nm.

SEND patterns were simulated using the phase object approximation [17] and a 5000-atom model $Zr_{36}Cu_{64}$ (4 nm × 4 nm × 4 nm) obtained using MD and embedded atom method potentials [18,19]. The experimental [Fig. 1(b)] and simulated [Fig. 1(c)] SEND patterns display diffracted intensities at the positions of the first and second diffraction rings for this glass (4.5 nm^{-1} and 8.0 nm^{-1}, respectively [19]) and a similar size of diffracted speckle to the undiffracted disc, demonstrating that a similar low number of local clusters is being probed in each case. Both the simulated and experimental patterns display a breakdown in absolute Friedel symmetry. In the case of the simulated SEND patterns with no aberrations and perfectly coherent illumination, the breakdown reflects the lack of centrosymmetry in the object function and is enhanced at low angle where the diffracted and undiffracted waves are of similar magnitude, as observed elsewhere [20]. The breakdown in Friedel symmetry in the experimental SEND patterns is further increased by uncompensated higher-order aberrations (for example, fivefold astigmatism), limited coherence [20,21], and a slightly increased experimental thickness. Figure 1(d) displays the simulated SEND pattern from an icosahedral cluster [18,19] oriented down its fivefold axis. A perfect icosahedron has thirty twofold, twenty threefold, and twelve fivefold symmetry axes, resulting in SEND patterns with distinct two-, six- and tenfold symmetries, respectively.

To quantify the symmetries present in each SEND pattern recorded at probe position $\vec{r} = (x, y)$, we calculated the four-point angular cross correlation function (CCF) defined by Wochner *et al.* [22] as a function of scattering vector magnitude, $|\vec{k}| = k = \sqrt{k_x^2 + k_y^2}$, according to

$$C_k(\vec{r}, k, \Delta) = \frac{\langle I(k, \phi) I(k, \phi + \Delta)\rangle_\phi - \langle I(k, \phi)\rangle_\phi^2}{\langle I(k, \phi)\rangle_\phi^2}. \quad (1)$$

Here, $I(k, \phi)$ is the intensity diffracted into a given k and azimuthal angle ϕ, and $\langle\rangle_\phi$ denotes averaging over the azimuthal angle at a given k [23]. This function and the related "correlograph" [24] have been employed to pick out subtle angular correlations in x-ray [22] and electron [24] diffraction speckle patterns, respectively. CCFs are displayed in Figs. 2(a), 2(d), and 2(g) for the experimental and simulated SEND patterns from glasses and the simulated SEND pattern from the single on axis icosahedron [Figs. 1(b)–1(d)], respectively. Profiles through the CCFs from the first diffracted ring are shown in Figs. 2(b), 2(e), and 2(h). The SEND patterns from the experimental and model glasses have prominent tenfold and sixfold symmetries, respectively, not obvious prior to CCF analysis, while the SEND pattern from the icosahedral cluster shows strong tenfold symmetry. In general, the SEND patterns from glasses possess a number of different symmetries at various k that vary greatly from point to point. Strong symmetries in the experimental SEND patterns are mostly confined to the first diffracted ring, as the signal-to-noise ratio at higher scattering angles is low as we see in the CCF in Fig. 2(a).

Altarelli and co-workers have analyzed the properties of the CCF assuming an orientationally disordered system of scatterers with prominent local structures [23,25]. They find that in the limit of either dilute systems or densely packed systems in which the illumination has a coherence length comparable to the size of the local cluster, as in this Letter, the CCF will demonstrate angular correlations reflecting symmetries of the local structural units [23,25]. Moreover, the magnitude of the symmetries present can be

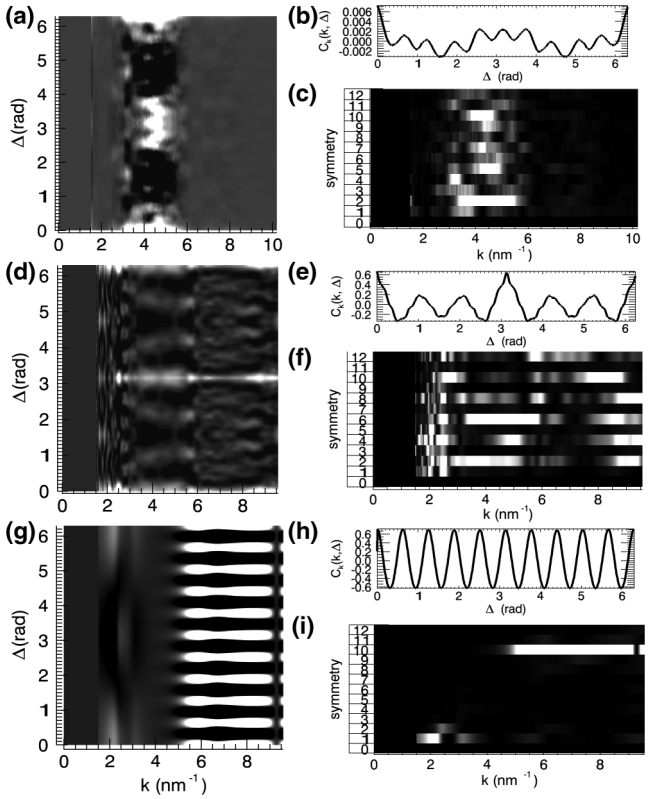

FIG. 2. Angular CCFs, profiles of these CCFs from k within the first diffracted ring, and magnitudes of the zero- to twelvefold symmetries in the CCFs from the experimental SEND pattern (a),(b),(c) and the simulated SEND patterns from the model glass (d),(e),(f) and icosahedral cluster (g),(h),(i). [Original SEND patterns displayed in Figs. 1(b)–1(d)].

accessed by decomposing the CCF at each k into a Fourier-cosine series [23]. We plot the Fourier coefficient of each symmetry in the SEND patterns as a function of k and show this symmetry magnitude in Figs. 2(c), 2(f), and 2(i) for the zero- to twelvefold symmetries. The appearance of odd symmetries in the symmetry magnitude images from the experimental and model glasses [Figs. 2(c) and 2(f)] confirms the earlier noted breakdown of Friedel symmetry to varying degrees, with the experimental symmetry magnitude image showing more intense odd symmetries at higher k than simulation.

Since we obtain the magnitude of each symmetry in each SEND pattern from a scanned array, we can (a) spatially average the symmetry magnitudes to investigate the nature of the predominant local structure and (b) map individual symmetry magnitudes to examine the spatial extent of particular symmetries. Such symmetry maps will reflect the degree to which adjacent local structures share prominent symmetry axes in this glass. We average the magnitude of the two-, six-, and tenfold symmetries over the width of the first diffraction ring ($3 \leq k \leq 6$ nm^{-1}) and map these averages. These maps are presented in Fig. 3 for the model [Figs. 3(a), 3(c), and 3(e)], and experimental [Figs. 3(b), 3(d), and 3(f)] glass with contrast ranges set to

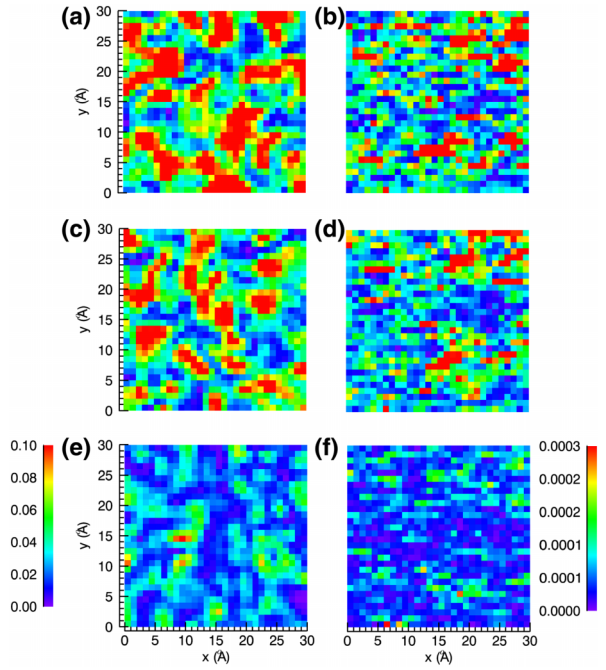

FIG. 3 (color online). Two-, six-, and tenfold symmetry maps produced from simulated (a),(c),(e) and experimental (b),(d),(f) SEND patterns from $Zr_{36}Cu_{64}$. Contrast for the simulated and experimental maps has been scaled to the maximum intensity in the tenfold maps.

the maximum intensity in the tenfold symmetry maps. The experimental maps are noisier, with overall much lower intensities than the simulated maps. This is due to camera noise in the experimental SEND patterns, ultimately circumscribed by mechanical stability of the specimen. However, there are strong similarities between the experimental and simulated maps in terms of contrast and intensity distribution with the twofold maps possessing a much higher intensity than the six- and tenfold maps. Generally, in scanning/transmission electron microscopy the experimental contrast is much less than the simulated contrast by a factor known as the "Stobbs factor" [10,26], whereas in this case, the contrasts compare well.

If icosahedral clusters dominate the SRO as suggested by modeling [4,19], the integrated intensities of the two-, six- and tenfold maps should reflect the ideal ratio of 30:20:12 for an assembly of randomly oriented icosahedra. For the simulated and experimental symmetry maps, the ratios of the total intensities was $31.6 \pm 1.2{:}25.6 \pm 0.2{:}12.0 \pm 0.4$ and $33.9 \pm 7.1{:}27.0 \pm 4.1{:}12.0 \pm 1.7$, respectively. The symmetry map intensities compare well to those for a dominant icosahedral SRO, confirming modeling [4,19]. The integrated sixfold intensities are elevated with respect to the ideal value for icosahedra, suggesting significant fractions of other polyhedral types that could be investigated by probing other symmetries.

We now demonstrate the spatial sensitivity of SEND to individual SRO clusters and investigate MRO by mapping.

We identified a low intensity region in the simulated tenfold symmetry map and placed an icosahedral cluster in that position aligned along its fivefold axis. We simulated the tenfold symmetry maps again using various probe sizes: $d_p = 0.82$, 0.51, 0.36 nm ($\alpha = 1.7$, 2.7, 4.0 mrad). We display the difference maps upon addition of the cluster in Figs. 4(a)–4(c). It is clear that the $d_p = 0.51$ probe, most closely matched to the cluster size, gives the most unambiguous intensity increase that is also the most spatially correlated to the cluster position. All probe sizes detect an increase in tenfold symmetry magnitude, indicating spatial sensitivity to on axis SRO clusters. For the 0.82, 0.51, and 0.36 nm probes, the percentage intensity increase in the pixel central to the cluster is 25%, 131%, and 27%, respectively. In the 5 pixel × 5 pixel area surrounding the cluster, the percentage intensity increases are 9%, 61%, and 4% in descending order of probe size.

The 0.51 nm probe is optimum, giving rise to SEND patterns in which prominent angular correlations reflect atomic correlations in the same local cluster with greater probability and without overlapping diffracted intensities, yielding symmetries not directly related to structure. Angular correlations between atoms in the same column but different clusters can result in serendipitous symmetries in SEND patterns. The SEND pattern from the cluster and glass together resembles that from the glass only; the increase in tenfold symmetry can only be detected with CCF analysis (see the Supplemental Material [15]). These observations draw into question the comparison of individual SEND patterns from a glass with a library of simulated patterns to identify polyhedral type and orientation [12]. We conclude with Gibson *et al.*, that for disordered structures in projection, the angular correlations in a single SEND pattern cannot be directly interpreted and must be related to the atomic order using statistical measures as we develop here [24].

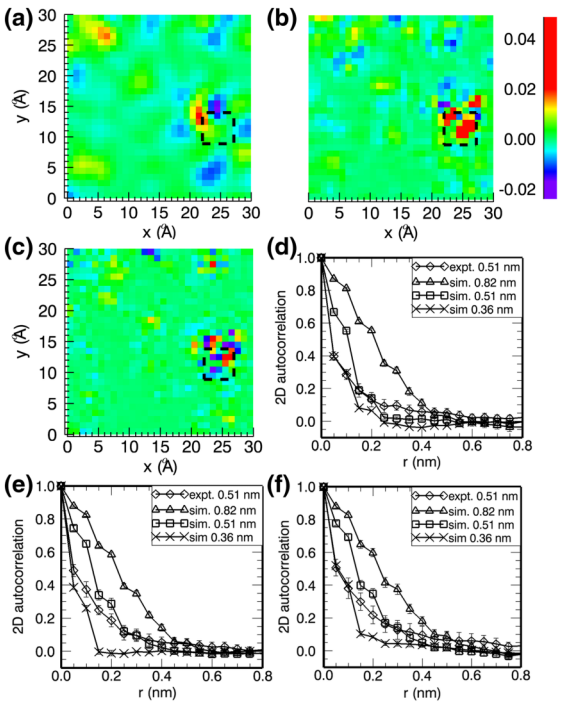

FIG. 4 (color online). Differences between tenfold symmetry maps with and without an icosahedral cluster placed at pixel (24, 11) for a probe size of (a) 0.82 nm, (b) 0.51 nm, and (c) 0.36 nm. Radially averaged 2D autocorrelation functions of (d) tenfold, (e) sixfold, and (f) twofold symmetry maps from the experimental data with $d_p = 0.51$ nm and the simulated maps for various d_p, respectively.

To quantify the spatial extent of the symmetries present in the SEND patterns, we calculated the radially averaged 2D-autocorrelation functions from the symmetry maps. In Figs. 4(d)–4(f), we display these functions for the tenfold, sixfold, and twofold symmetry maps from the experimental data and simulations with a range of probe sizes. In all cases, except the experimental twofold map, the autocorrelation function decays to zero within the FWHM of the probe, indicating that in general, there are no correlated regions larger than the probe sizes. The final radial distance where the autocorrelation function is above zero outside error is 0.55 nm, 0.55 nm, and 0.85 nm for the experimental ten-, six-, and twofold maps and 0.40 nm, 0.45 nm, and 0.45 nm for the simulated ten-, six-, and twofold maps with the 0.51 nm FWHM probe, respectively.

The lack of correlation in the experimental ten- and sixfold maps, and increased correlation length in the twofold map implies a face-sharing or interpenetrating MRO for the icosahedra, since in these configurations, and in contrast to edge- and vertex-sharing configurations, adjacent icosahedra will not share any of their five- or threefold axes (see the Supplemental Material [15]). Adjacent icosahedra in a face-sharing or interpenetrating configuration will have six and ten instances of two twofold axes sharing a normal direction, respectively, giving rise to the observed increase in the twofold map correlation length. The simulated symmetry maps for all probe sizes do not show an increased correlation length for any of the symmetries. This divergence from the experimental data is consistent with less developed MRO due to the million times greater model quench rate compared to the melt-spun glass.

A glass structure dominated by face-sharing and interpenetrating icosahedra is in accord with efficient space filling [27] and provides support for modeling studies that find a structural basis for the glass-forming ability of this system [7]. Analysis of a glass model of the same composition as examined in this Letter using cluster alignment, discovered an MRO of Bergman-type clusters (icosahedral-dodecahedral-icosahedral shells around a central Cu atom) [28]. This is equivalent to interpenetrating icosahedra in which the vertex of one icosahedron is the center of another. Models of $Zr_{50}Cu_{45}Al_5$ generated by FEM-constrained RMC calculations discovered crystal- and icosahedral-like superclusters 0.7–1.0 nm in size [10].

Our analysis does not detect crystal-like superclusters with sixfold symmetry. Although an extended correlation length in the twofold symmetry map provides evidence of the existence of icosahedral superclusters in a face-sharing or interpenetrating configuration, significant further modeling will be required to extract the supercluster size from this measurement (see the Supplemental Material [15]). However, using a naive treatment, in which we relate the correlation length (adjusted for broadening due to the finite probe size) to the radius of gyration [29], R_g, of rectangular superclusters with a width (W) equal to the cluster diameter and a length (L) proportional to the number of face-sharing or interpenetrating clusters, then we obtain $R_g^2 = (0.85)^2 - (0.51)^2 = 1/3[(W/2)^2 + (L/2)^2]$. This yields an estimate of four clusters in a face-sharing configuration or seven in an interpenetrating configuration. However, the correlation length measured from persistent angular symmetries in coherent scanning electron nanodiffraction patterns may not have this simple relationship to the average supercluster size.

Through the statistical analysis of magnitude maps of angular symmetries in experimental and simulated SEND patterns, we demonstrated that the dominant SRO in a melt-spun $Zr_{36}Cu_{64}$ glass was consistent with icosahedral clusters. Analysis of the spatial extent of prominent angular symmetries in the maps suggests a face-sharing or interpenetrating model of MRO. Measuring the extent of this MRO from symmetry map correlation lengths and estimating the size of string-like features will require further modeling. Nevertheless, mapping the strength of angular correlations in SEND patterns is a promising direct technique for the study of disordered materials.

A. C. Y. L. gratefully acknowledges the support of the Science Faculty and the Monash Centre for Electron Microscopy (MCEM), Monash University. The electron microscopy was performed at the MCEM. We thank Mr. Renji Pan, Dr. Russell King, Dr. Xi-Ya Fang, and Dr. Matthew Weyland of the MCEM for their assistance. The FEI Titan^3 80-300 FEGTEM was funded by the Australian Research Council (Contract No. LE0454166). Samples were prepared and MD simulations were performed at Ames Laboratory, funded by the U.S. Department of Energy, Office of Basic Energy Sciences, Division of Materials Sciences and Engineering under Contract No. DE-AC02-07CH11358. We thank Dr. M. Besser and Dr. M. Mendelev for their contributions, and Associate Professor David Paganin and Dr. Scott Findlay for contributions when preparing the manuscript.

*amelia.liu@monash.edu

[1] D. B. Miracle, Nat. Mater. **3**, 697 (2004).
[2] N. Mattern, A. Schöps, U. Kühn, J. Acker, O. Khvostikova, and J. Eckert, J. Non-Cryst. Solids **354**, 1054 (2008).
[3] Y. Q. Cheng, H. W. Sheng, and E. Ma, Phys. Rev. B **78**, 014207 (2008).
[4] X. W. Fang, C. Z. Wang, Y. X. Yao, Z. J. Ding, and K. M. Ho, Phys. Rev. B **82**, 184204 (2010).
[5] M. Li, C. Z. Wang, S. G. Hao, M. J. Kramer, and K. M. Ho, Phys. Rev. B **80**, 184201 (2009).
[6] F. C. Frank, Proc. R. Soc. A **215**, 43 (1952).
[7] S. G. Hao, C. Z. Wang, M. Z. Li, R. E. Napolitano, and K. M. Ho, Phys. Rev. B **84**, 064203 (2011).
[8] Y. Shi and M. L. Falk, Phys. Rev. Lett. **95**, 095502 (2005).
[9] M. M. J. Treacy and K. B. Borisenko, Science **335**, 950 (2012).
[10] J. Hwang, Z. H. Melgarejo, Y. E. Kalay, I. Kalay, M. J. Kramer, D. S. Stone, and P. M. Voyles, Phys. Rev. Lett. **108**, 195505 (2012).
[11] J. Wen, Y. Q. Cheng, J. Q. Wang, and E. Ma, J. Appl. Phys. **105**, 043519 (2009).
[12] A. Hirata, P. Guan, T. Fujita, Y. Hirotsu, A. Inoue, A. R. Yavari, T. Sakurai, and M. Chen, Nat. Mater. **10**, 28 (2010).
[13] J.-M. Zuo and J. Tao, in *Scanning Transmission Electron Microscopy*, edited by S. J. Pennycook and P. D. Nellist (Springer, New York, 2011), p. 393.
[14] J. M. Cowley, Ultramicroscopy **90**, 197 (2002).
[15] See Supplemental Material at http://link.aps.org/supplemental/10.1103/PhysRevLett.110.205505 for details of thickness determination using electron energy loss spectroscopy; selected area diffraction; models of MRO; simulations showing the technique's sensitivity to icosahedral SRO in the glass from CCF analysis; and the extent of face-sharing clusters (MRO) from the correlation length in the twofold symmetry map.
[16] R. F. Egerton, *Electron Energy-Loss Spectroscopy in the Electron Microscope* (Plenum, New York, 1996), 2nd ed.
[17] E. J. Kirkland, *Advanced Computing in Electron Microscopy* (Springer, New York, 2010), 2nd ed.
[18] M. I. Mendelev, M. J. Kramer, R. T. Ott, D. J. Sordelet, D. Yagodin, and P. Popel, Philos. Mag. **89**, 967 (2009).
[19] M. I. Mendelev, M. J. Kramer, R. T. Ott, D. J. Sordelet, M. F. Besser, A. Kreyssig, A. I. Goldman, V. Wessels, K. K. Sahu, K. F. Kelton, R. W. Hyers, S. Canepari, and J. R. Rogers, Philos. Mag. **90**, 3795 (2010).
[20] M. J. Hÿtch and J. P. Chevalier, Ultramicroscopy **58**, 114 (1995).
[21] J. M. Rodenburg, Ultramicroscopy **25**, 329 (1988).
[22] P. Wochner, C. Gutt, T. Autenrieth, T. Demmer, V. Bugaev, A. D. Ortiz, A. Duri, F. Zontone, G. Grübel, and H. Dosch, Proc. Natl. Acad. Sci. U.S.A. **106**, 11511 (2009).
[23] M. Altarelli, R. P. Kurta, and I. A. Vartanyants, Phys. Rev. B **82**, 104207 (2010).
[24] J. M. Gibson, M. M. J. Treacy, T. Sun, and N. J. Zaluzec, Phys. Rev. Lett. **105**, 125504 (2010).
[25] R. P. Kurta, M. Altarelli, E. Weckert, and I. A. Vartanyants, Phys. Rev. B **85**, 184204 (2012).
[26] A. Howie, Ultramicroscopy **98**, 73 (2004).
[27] P. M. Ossi, *Disordered Materials: An Introduction* (Springer, New York, 2006), 2nd ed., p. 164.
[28] X. W. Fang, C. Z. Wang, S. G. Hao, M. J. Kramer, Y. X. Yao, M. I. Mendelev, Z. J. Ding, R. E. Napolitano, and K. M. Ho, Sci. Rep. **1**, 194 (2011).
[29] J. M. Gibson, M. M. J. Treacy, and P. M. Voyles, Ultramicroscopy **83**, 169 (2000).